A comparative study of wind turbine rotor aerodynamic loads obtained from an experimental approach and predicted by a high fidelity CFD simulation

Mylène Dumanoir, Annie Leroy, Emmanuel Guilmineau, Stéphane Loyer, Azeddine Kourta

Association Aéronautique et Astronautique de France

58th 3AF International Conference on Applied Aerodynamics
27 — 29 March 2024, Orléans – France

AERO2024-ID-NAME

A comparative study of wind turbine rotor aerodynamic loads obtained from an experimental approach and predicted by a high fidelity CFD simulation

Mylène Dumanoir[(1)], Annie Leroy[(1)], Emmanuel Guilmineau[(2)], Stéphane Loyer[(3)] and Azeddine Kourta[(3)]

[(1)]*Centre de Recherche de l'École de l'Air, B.A. 701, 13661 Salon-Air, France, annie.leroy@ecole-air.fr*

[(2)]*Ecole Centrale de Nantes, LHEEA, 1 rue de la Noë, 44321 Nantes, France, emmanuel.guilmineau@ec-nantes.fr*

[(3)]*Univ. Orléans, INSA-CVL, PRISME EA4229, 45072 Orléans, France, azeddine.kourta@univ-orleans.fr*

ABSTRACT

Computational prediction of aerodynamics for a two-bladed wind turbine rotor model at the profile, blade, and rotor scale are compared to experimental data. It is measured at the wind tunnel of the University of Orleans with an instrumented rotor model to obtain global coefficients, bending moments, and pressure chordwise distributions. A turbulence grid is used to obtain a turbulence intensity of 3.8% at the rotor position. A $k-\omega$ SST unsteady Reynolds-averaged Navier-Stokes (URANS) model is conducted with a fully resolved rotor, with and without automatic grid refinement. This study aims to examine the prediction capabilities of the simulation for various physical variables. The simulation demonstrates a relatively good prediction of power and thrust coefficients compared with experimental data with a maximum scatter of 8.5%. The prediction of the pressure coefficient distribution at three different radial positions is satisfactory but shows discrepancies when it comes to accurately predicting flow separation and Reynolds effects.

1. INTRODUCTION

In wind farms, wind turbines are subject to turbulent flows resulting from upstream wind conditions and wakes. The concomitant presence of three-dimensional, rotational, turbulent effects, or even separated flows makes the flow fields highly complex. The prediction of rotor aerodynamics in such conditions must be reliable as it is directly related to wind turbine performances and therefore to the estimation of fatigue of the latter. Numerical modeling for the analysis of rotor aerodynamics will need to rely on a new generation of high-fidelity modeling [1] accompanied by increasingly complex experimental configurations and on-site measurements.

Bartl and Sætran [2] worked on the effects of various turbulent inflow conditions on a row of two wind turbines. By comparing experimental and numerical results, their study focused on evaluating the performances of both wind turbines and to assess wake velocity deficit. One of their results showed that the turbulence effect generated by a passive grid on the power and thrust coefficients is well predicted by $k-\omega$ SST turbulence model among RANS models. To extend the previous study, Chen *et al.* [3] carried out a fully resolved rotor ID-DES simulation. They found that the mean power and thrust coefficients agreed well with existing experimental data. It is also shown that turbulence had few impacts on these latter coefficients except in shear inflow conditions. Krogstad and Lund [4] compared experimental and numerical results on predicting wind turbine model performances. The numerical predictions are considered satisfactory compared to the experimental results despite overestimating the power coefficient for tip speed ratios greater than 6. This can be explained by difficulties in estimating blockage effects and drag force. Moshfeghi *et al.* [5] compared experimental and numerical results to study the aerodynamic behavior at different scales for their cases. The SST-$k-\omega$ seems to fail to predict the separation point emergence. The thrust values are mispredicted for highly separated flows. They suggested paying particular attention to the number of nodes in the chordwise and spanwise directions, close to the surface. Lee *et al.* [6] conducted the same type of comparison using a twisted and non-twisted blade. With the twisted blade a better optimum power coefficient is unsurprisingly obtained because it is designed to alleviate separated flows. This brief literature review shows that further efforts are still required to make progress in the develop-

ment of high-fidelity modeling.

This paper is part of a project that aims to make further progress in the development of reliable CFD tools for studying and predicting rotor aerodynamics and aeroelasticity. Prior to proceeding to simulations with higher and more realistic Reynolds number, the initial step is to compare characteristic physical quantities derived from high-fidelity 3D URANS simulations and measured from wind tunnel experiments performed on a wind turbine model under turbulent inflow conditions. Sensors are fitted on this model to get data at the airfoil, blade, and rotor scales.

First, a comprehensive description of the wind turbine experimental model and its testing environment are presented, offering sufficient information to enable the setup of a numerical simulation. Then, the focus shifts to the parameters of this simulation. Secondly, a comparison is presented between the numerical results and the measured data obtained from the wind tunnel investigation, with particular emphasis on the turbulent inflow conditions. Afterward, the paper is concluded with key findings and future perspectives.

2. METHODS

2.1 Experimental setup

The experiments are performed in a closed-loop large subsonic wind tunnel. The wind turbine model (visible in figure 1) is positioned in the return test section at the exit of a convergent which has a section of 3×3 m^2.

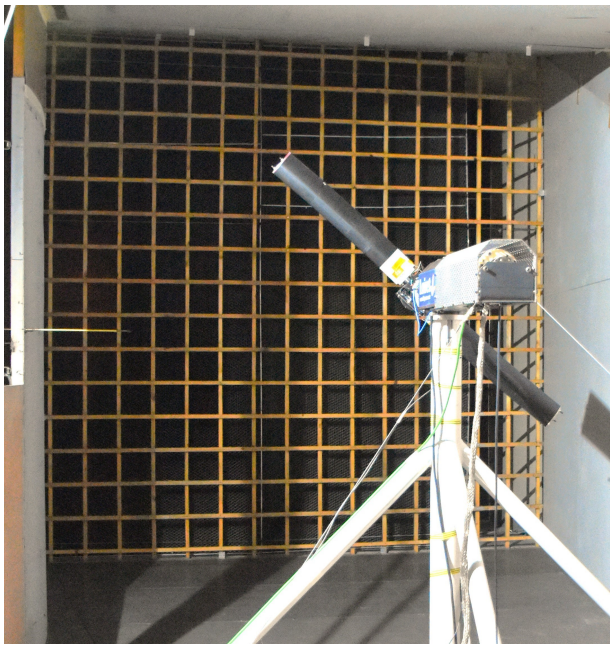

Figure 1: Turbulence grid and wind turbine model.

The incoming wind speed $U_{\infty,exp}$ is controlled by one Pitot probe located at 0.3 m of the wind tunnel wall and 1 m upstream of the rotor, and by a second one in the main test section. From these two probes, it is possible to assess the blockage effect. Each acquisition being unique, the upstream velocity $U_{\infty,exp}$ is specified in table 1. A passive and uniform turbulence grid is used as shown on figure 1. According to Wagner *et al.* [7], the turbulent intensity TI varies from 2 to 8% on-shore. This grid made it possible to achieve a case at TI=3.8%. The bar width b and the mesh size M are equal to 25 and 225 mm respectively. The turbulence grid is characterized using hot wire anemometry at the rotor position without the wind turbine model in the test section. A ProCap system was also used to characterize the field upstream of the rotor. This system is a hand-guided 5-hole pressure probe iProbe from Vectoflow GmbH, fitted with 500 Pa pressure sensors [8]. Thanks to the reflective passive markers, its instantaneous position is captured in real-time by the infrared cameras placed at the upper left of the return section when looking upstream. A zero-velocity offset correction was performed before each measurement. The spatial resolution for the hand-guided and the traverse system measurements was set to 50 and 25 mm respectively. The ProCap measurements presented were made with the rotor locked in the horizontal position and also in rotation. The velocity of the probe is corrected in the data for all cases by the ProCap software. Real-time viewing allows the operator to return on areas where acquisitions are insufficient. More precision is provided in section 3.1. The distance grid-rotor d is $2.7D$. The wind turbine bench has a hub height of 1.56 m. Designed to measure its performance and its local aerodynamic properties by measuring the chordwise pressure distribution at various radial positions [9], the wind turbine bench is equipped with two untwisted and untapered blades with a rotor diameter D of 1.4 m and a swept rotor surface S_{rotor} of 1.54 m^2. The airfoil section is a NACA 65_4-421 with a chord length c of 0.1 m, slightly modified at the trailing edge for Baleriola works [10].

The turbine rotates counter-clockwise when the observer is facing the wind. To have the same order of magnitude in tip speed ratio $\lambda = \frac{\Omega r}{U_\infty}$ [11] as full-scale rotors, the wind turbine bench is made up of a reversible motor Phase Ultract 509 that enables the monitoring of the turbine rotational velocity up to 1000 rpm. Thus, a kinematic scaling is chosen. The servomotor provides energy when the working point of the turbine is propulsive and dissipates energy when the working point is extractive (present case).

The blade is equipped with several sensors. Placed at the rear of the turbine, the torque and thrust of the wind turbine are measured with a Scaime M2392 transducer. For the flapwise bending moment M_{fbm}, Kyowa strain gages full bridge circuit are placed at the roots of the two blades. 27 pressure taps measure the mean

Table 1: Sampling parameters. Abbreviations: No_{rev} for rotor revolution number, HWA for hot wire anemometry. $U_{\infty,exp}$ is obtained at the test section center with HWA (*) or at $\lambda = 0$ with the Pitot probe (**).

	Measurement means	Sampling freq. [Hz]	No. of samples	Acquisition time per sample	$U_{\infty,exp}$ $\left[m.s^{-1}\right]$
Sweeping (fig. 3)	HWA	10 000	65 536	6.5 s	-
Mapping (fig. 4)	HWA	10 000	65 536	17.5 s	9.85*
Mapping (fig. 5,7)	ProCap	50	-	-	9.53
Torque, thrust, M_{fbm}	See sect. 2.1	500	15 000	No_{rev} = 0 - 400	9.18**
C_p	See sect. 2.1	500	15 000	No_{rev} = 150, 400	10.26**

pressure distribution. They are placed on one of the two blades in chordwise at three different possible radial positions r/R: 38, 65, and 88%. The taps are connected to a 32-channel differential pressure scanner ESP-32HD (GE, $\pm$0.361 PSI) embedded in a MicroDAQ system (CHELL). To have the best power coefficient $C_{power,max}$, a pitch angle β of 4° is chosen. The experimental acquisition parameters are given in Table 1.

2.2 Numerical setup

Numerical simulations are carried out by the flow solver ISIS-CFD, developed by CNRS and Centrale Nantes. An incompressible unsteady Reynolds-Averaged Navier-Stokes (URANS) simulation is performed using $k-\omega$ SST model for turbulence closure.

Based on the finite volume method, the solver builds the spatial discretization of the transport equations. The unstructured discretization is face-based. A second-order backward difference scheme is used to discretize time. The velocity field is obtained from the momentum conservation equations and the pressure field is extracted from the mass equation constraint, or continuity equation, expressed into a pressure equation. Transport equations for the variables in the turbulence model are added to the discretization [12]. The full rotor geometry with the hub and a part of the nacelle is resolved in its frame of reference. The simulations are carried out with a rotating frame method which means that the equations are written in the rotor frame. The computational domain consists of a cylindrical domain whose diameter is 10 m $= 7.14D$, and the height is 14 m $= 10D$, with D the rotor diameter. The inlet is located at 2.8 m $= 2D$ in front of the rotor plane. At the inlet and the external boundary of the computational domain, a Dirichlet condition is used while at the outlet the pressure is imposed. For the blades and the shaft, a no-slip condition is used and for the rotation axis it is a wall function. The upstream velocity is fixed to $U_{\infty,num} = 9.38$ m/s.

The mesh is generated with Hexpress™, an automatic unstructured mesh generator that generates meshes containing only hexahedrons. The mesh consists of 18.6 $\times$ 10^6 points. The number of faces to represent the geometry is 5.7 $\times$ 10^5 with 2.5 $\times$ 10^5 faces for each blades. The average wall normal resolution on the blades is y^+ = 0.6 while for the shaft the value is 0.2 and for the rotation axis 3.3. The automatic grid refinement (AGR) is activated for few rotation velocities and the mesh depends on the chosen tip-speed ratio. AGR in ISIS-CFD is performed by local division of unstructured hexahedral meshes [13]. The decision where to refine is based on a metric refinement criterion, a tensor field computed from the flow. The tensor is based on the second derivative of the flow variables. The refinement criterion is the flux-component Hessian. The grid is refined until the dimension of each cell satisfy the threshold Tr and the appropriate mesh density is specified by the minimum cell size. Figure 2 represents the variation of the mesh with and without AGR. It should be noted that the mesh without AGR is the same whatever the radial position r but varies for mesh with AGR.

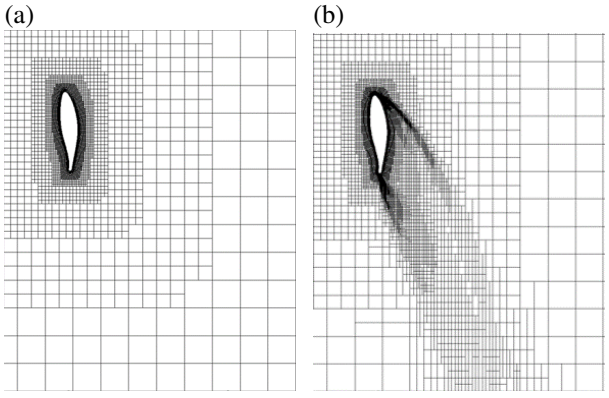

Figure 2: Meshes r without (a) and with AGR at the radial positions r=0.63R (b) for $\lambda = 2.4$

The time step for all cases is 0.025 s. The table 2 gives information for 3 tip-speed ratios λ.

Table 2: Simulation parameters

λ	No. cells	No. faces on one blade	No_{rev}
0.0	37.9×10^6	4.0×10^5	0
2.4	42.4×10^6	8.2×10^5	500
5.5	32.7×10^6	4.5×10^5	800

3. RESULTS AND DISCUSSION

3.1 Inflow conditions

The first step is to characterize the upstream turbulent flow obtained by the passive grids. Three-component hot-wire measurements allow the calculation of turbulence intensities defined as follow:

$$TI_u = \frac{\sqrt{\overline{u'^2}}}{\sqrt{\overline{U^2}+\overline{V^2}+\overline{W^2}}}, \quad TI_v = \frac{\sqrt{\overline{v'^2}}}{\sqrt{\overline{U^2}+\overline{V^2}+\overline{W^2}}},$$

$$TI_w = \frac{\sqrt{\overline{w'^2}}}{\sqrt{\overline{U^2}+\overline{V^2}+\overline{W^2}}}, \tag{1}$$

where U,V,W and u',v',w' stand for the mean and the fluctuation of the components of velocity respectively, according to a reference coordinate system based on the streamwise x-direction. $\overline{(.)}$ denotes time averaging. To simplify the notation, the longitudinal turbulence intensity TI_u will be denoted as TI, and all time-averaged velocity components will be noted without the bar.

Figure 3 shows the evolution of the turbulence intensity TI in the nondimensional streamwise direction x/D. These measurements are carried out before the installation of the wind turbine model. The black vertical dashed line marks the position of the rotor plane.

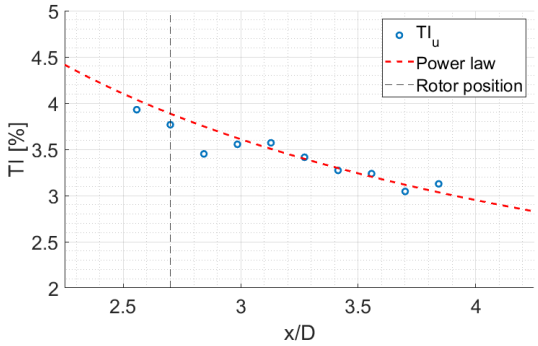

Figure 3: Turbulence intensity TI as function of x/D. $x/D = 0$ corresponds to the position of the grid.

The measurements allow to check a decay in the turbulent intensity TI. When a passive turbulence grid is used, the turbulence generated is divided into two regions: the production region and the decay region. The first, located directly after the grid, is associated with an increase of the turbulence intensity, unlike the decay region. Furthermore, the measurements are rather well approximated by the following power law [14]:

$$TI \sim C\left(\frac{x}{M}\right)^{-n}. \tag{2}$$

C and n are values determined experimentally. Here, 0.7 is found for n and other authors also found this same value [15][16]. The turbulence intensity of 3.8% is obtained at the rotor position with an integral turbulent length scale of 7.4 cm and a Taylor microscale of 0.7 cm.

Figures 4(a) and (b) show velocity $U/U_{\infty,exp}$ and turbulent intensity TI maps respectively 2.6D downstream of the grid, in the (y,z) plane. The swept section is 1×1 m^2. The rotor area is marked with a white circle.

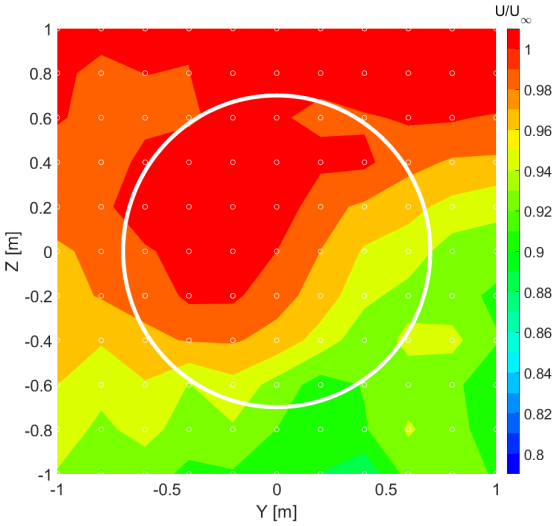

(a)

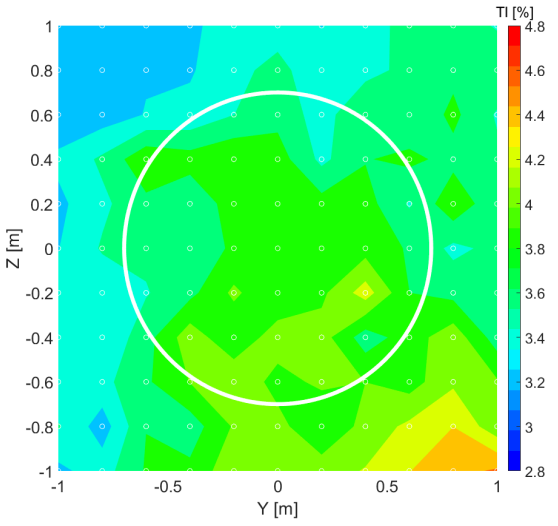

(b)

Figure 4: Velocity field $U/U_{\infty,exp}$ (a) and turbulent intensity field TI (b)

In figure 4(a), a velocity gradient is visible with lower

velocity $U/U_{\infty,exp}$ towards the bottom. This is also the case in the disc area. This is explained by the fact that the section studied faces a flow accelerated by a convergent built on flat ground. However, the scatter remains less than 10%. Concerning figure 4(b), the turbulent intensity TI is uniform in the rotor disk. Indeed, table 3 lists the extreme deviations observed in the rotor disk for the three components of velocity.

Table 3: Turbulent intensities TI and velocities (U,V,W) according to the 3 components

Directions	TI_{min}	TI_{max}	Velocities
Free-stream flow	3.4%	4.2%	$U \pm 0.1$ m/s
Transverse	3.5%	3.9%	0 ± 0.1 m/s
Vertical	3.7%	4.0%	0 ± 0.1 m/s

An overall turbulent intensity of approximately 3.8% is obtained in the three directions. Velocities V and W are about 0 m/s. In addition, the maximum absolute deviation for turbulent intensities and velocities is 10% whatever the direction of the flow. Thus, the measurements are carried out in the decay region, and the rotor plane position will be subject to a shear turbulent flow. It is assumed that the flow is nearly homogeneous and isotropic on the rotor area.

The figure 5 represents the nondimensional mean flow components U, V, W recorded by ProCap and the velocity profiles U for $x/D = 2.6$ (corresponding to 3.6 m) in the induction zone at $y/D = 0$.

The velocity gradient is still visible when looking at the U-velocity field. A blockage zone is distinguished by a low-speed bubble upstream of the hub. It starts at around $x = 3.5m$. The graph of the velocity profiles U makes it possible to characterize the gradient. As a reminder, the ProCap measurement was made in the presence of the rotor with the blades blocked horizontally, unlike the hot wire anemometry displayed on this graph. A power law is a common way of describing this visibly sheared flow. This power law is defined as follows:

$$\frac{u(z)}{u(z_{ref})} = \left(\frac{z}{z_{ref}}\right)^{\alpha} \tag{3}$$

with z_{ref} an arbitrary reference height. In the graph of the figure 5, the curve of the power curve is plotted in yellow. The value of 0.11 for α is chosen as a reference on Bartl and Sætran blind test comparison work [2]. This value was chosen based on the paper of Hsu *et al.* [17] which determined this coefficient (± 0.03) for offshore boundary layers in stable atmospheric conditions. The two means of measurement are rather in agreement with the power law. However, for the ProCap measurement, a gap is observed for $z > 0.3$ m. This is due to the presence of the rotor and therefore the blockage effect is also visible on the velocity field U. Concerning the V and W velocity fields, the absolute deviation is less than 0.05 m/s except near the hub.

To obtain the same turbulent intensity TI at the rotor plane in the simulation, according to Mishra *et al.* [18], the turbulent intensity TI of 23.2% with a Taylor scale of 0.0031 m are imposed at the inlet of the computational domain. Figure 6 shows longitudinal velocity maps with the rotor, positioned horizontally with zero rotation speed.

The blocking effect due to the presence of the rotor seems to be well captured by the numerical simulation. Indeed, an oval and horizontally elongated velocity U deficit zone corresponds to the presence of the rotor in

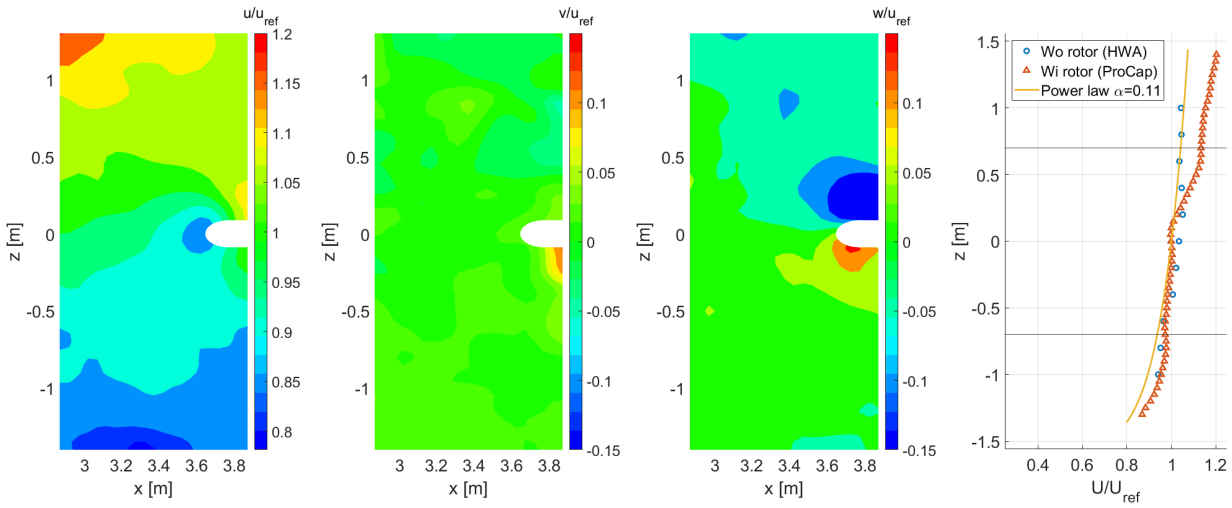

Figure 5: Velocity components $U/U_{\infty,exp}$, $V/U_{\infty,exp}$ and $W/U_{\infty,exp}$ field recorded with ProCap system.

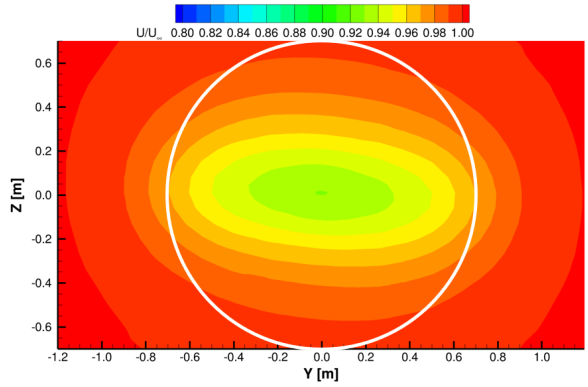

Figure 6: Velocity field U/U_∞ with the rotor at 2.6D downstream of the grid obtain by CFD.

a stationary position. As a reminder, the mast is not modeled in the simulation.

In order to evaluate the influence of the mat and the induction effect in the wind tunnel, figures 7(a) and (b) show the dimensionless velocity fields U/U_∞ in the plane (y,z) for a zero tip-speed ratio λ and $\lambda = 2.2$ respectively.

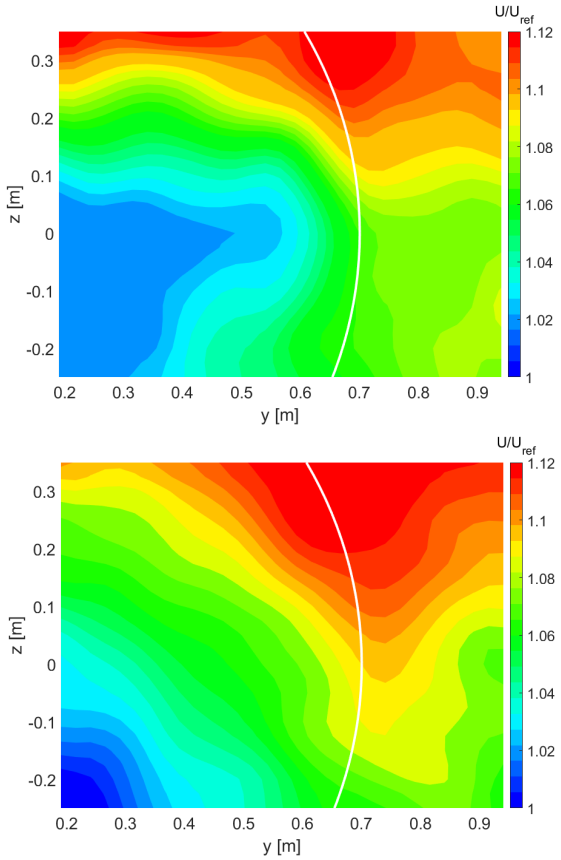

(a)

(b)

Figure 7: Velocity field U/U_∞ for locked (a) and rotating (b) rotor recorded with ProCap system.

In figure 7(a), the blocking effect due to the presence of the rotor locked in a horizontal position is perfectly recognizable. Furthermore, unlike the figure 6, a large low-speed area is visible under the rotor lock trace. There is therefore a blocking effect from the presence of the mast upstream of the flow. Concerning the case with the rotating blade, the induction effect is remarkable by the movements and the intensity of the extreme velocity zones. Indeed, in figure 7(b), approaching the axis of revolution of the turbine, the U-velocity was slowed down more than the case without rotation, marked by a more intense blue area. The opposite happens on the periphery of the rotation zone delimited by the white circle.

3.2 Performance of the wind turbine model

3.2.1 Aerodynamics at rotor scale

First, the global variables, i.e. the power and torque, are compared. For this purpose, those values are nondimensionalized using the following formulas:

$$C_{power} = \frac{Q\Omega}{\frac{1}{2}\rho U_\infty^3 S_{rotor}} \quad (4) \qquad C_{thrust} = \frac{T}{\frac{1}{2}\rho U_\infty^2 S_{rotor}} \quad (5)$$

where Q is the torque, T the overall drag, ρ the air density, U_∞ the incoming wind velocity, S_{rotor} the rotor swept area and Ω the rotational velocity of the turbine.

Figures 8 show a comparison of the power coefficient C_{power} (a) and the thrust coefficient C_{thrust} (b) between experimental and numerical results as a function of the tip-speed ratio λ. For the legend, the labels 'Wi AGR' and 'Wo AGR' stand for with and without AGR meshing respectively. This latter remark will applied for the rest of the paper.

The prediction is satisfactory for the power coefficient C_{power} from $\lambda = 0$ to $\lambda = 5.0$. For the experimental data, the optimal operating point of the turbine is obtained for a tip-speed ratio λ equal to 5.6. From this value of λ, a slight divergence is observed. It corresponds to a maximum power coefficient $C_{power,max}$ equal to 0.338 compared to simulations with $C_{power,max} = 0.363$ at $\lambda_{opt} = 5.8$. The scatter $\Delta C_{power,max}$ is about 7.4% between these last two values. This discrepancy can be explained by the difference in inlet velocities U_∞. Indeed, it is observed that in a wind tunnel, a 10% reduction in U_∞ leads to a reduction in λ_{opt} of about 12% and $C_{power,max}$ is smaller and vice versa. Focusing on the simulations, the numerical results with AGR and without AGR are superimposed, meaning that the AGR meshing does not seem to have any significant impact on these global variables for the tested configuration.

Regarding C_{thrust}, the prediction deviates more and more from the experimental measurements from $\lambda = 1.2$ but remains acceptable, even for large tip-speed ratios λ.

(a) (b)

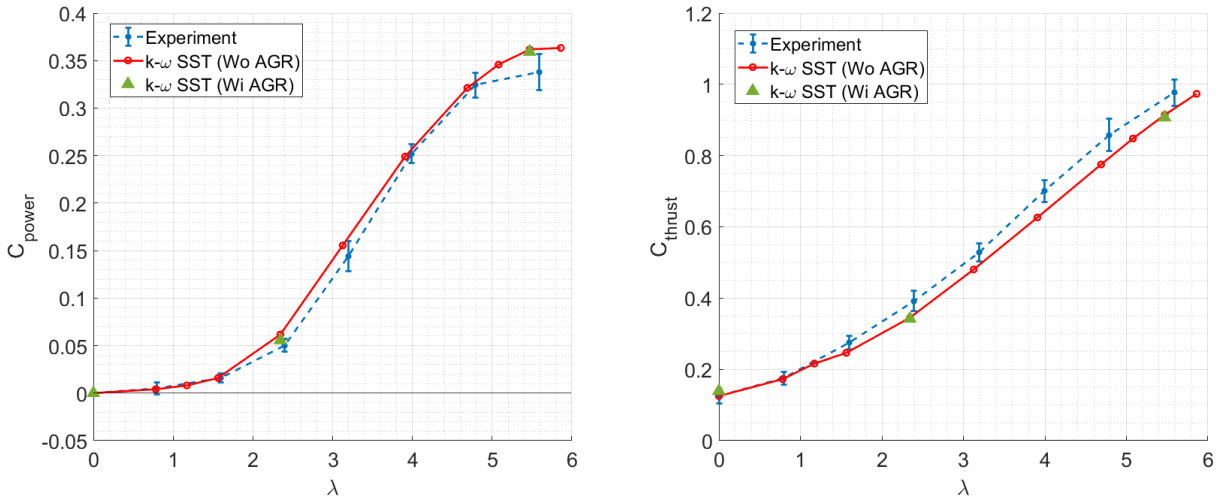

Figure 8: Power coefficient C_{power} (a) and thrust coefficient C_{thrust} (b)

3.2.2 Aerodynamics at blade scale

First, the flapwise bending moment M_{fbm} on blade roots are plotted. Figure 9 shows the latter as a function of the tip-speed ratio λ. Only the M_{fbm} for either blade is shown for ease of reading.

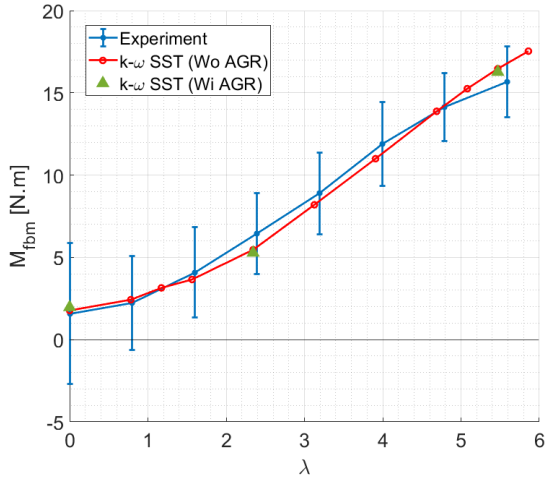

Figure 9: Flapwise bending moment M_{fbm} for two blades

The experimental results are well predicted by the simulation. The greater the rotation speed, the more the M_{fbm} increases. Indeed, the blades undergo increasing aerodynamic and mechanical efforts. The fluctuation for the experimental results generally remains constant. The distribution of mass and inertia along the blades is not uniform because of the implementation of pressure taps and tubes. Slight vibrations have been observed depending on the rotational velocity. This is not taken into account in the simulation and may explain some of the observed discrepancies. The numerical simulation has a maximum relative gap of about 7.1%. However, two areas are notable from $\lambda = 1.2$:

- for $\lambda = [1.2, 4.8]$, the M_{fbm} is underestimated by the simulation
- for $\lambda > 4.8$, the M_{fbm} is overestimated by the simulation.

The AGR mesh does not seem to have any impact on this physical variable either.

3.2.3 Aerodynamics at airfoil scale

The pressure measurements make it possible to obtain a chordwise pressure distribution at three different radial positions r and give access to local information on the aerodynamics of the blade profile. In this section, the pressure coefficient C_p distributions are compared. The pressure coefficient C_p is expressed as follow:

$$C_p = \frac{p - p_\infty}{\frac{1}{2}\rho(U_\infty^2 + (\Omega r)^2)} = \frac{p - p_\infty}{\frac{1}{2}\rho W_r^2}. \quad (6)$$

with p the local pressure, p_∞ the freestream pressure, and r the radial position.

Figures 10 show the C_p distribution as a function of the radial position r for a low and a high λ. dashed, continuous, and mixed lines stand for the experimental, the numerical without AGR, and with AGR results respectively. The tip-speed ratios of experimental λ_{exp} and numerical λ_{num} are specified, as well as the geometrical angle of attack for each section.

(a) $\lambda_{num} = 2.4$, $\lambda_{exp} = 2.2$ (b) $\lambda_{num} = 5.5$, $\lambda_{exp} = 5.7$

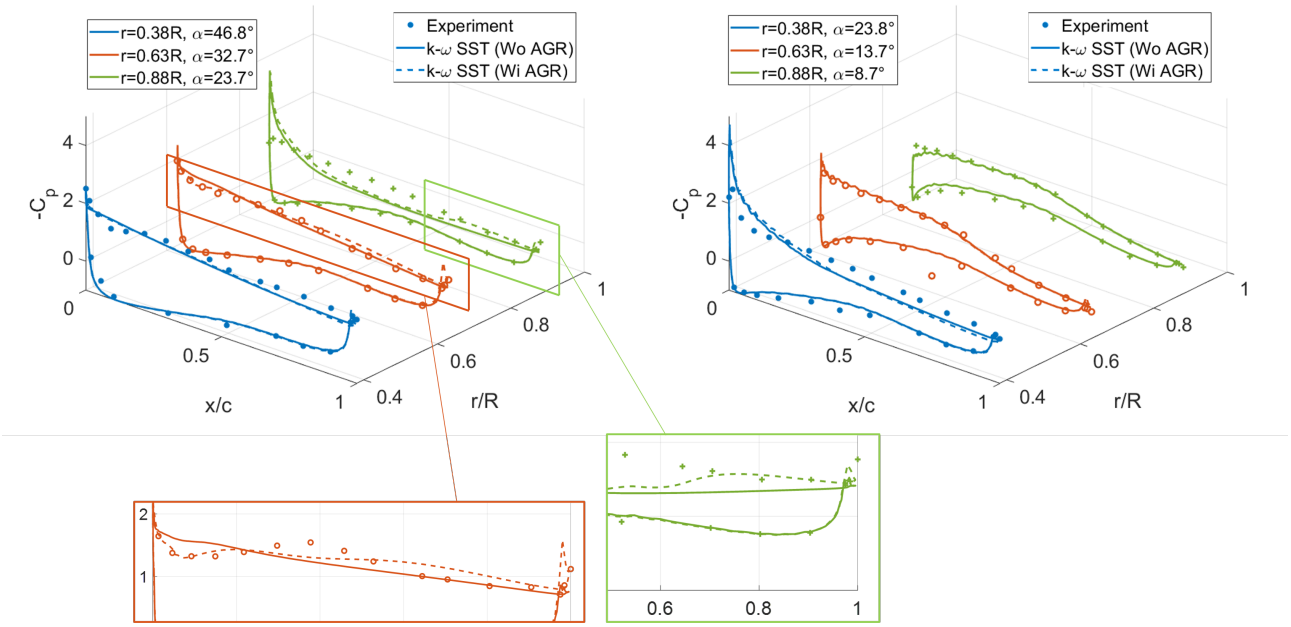

Figure 10: Pressure coefficient C_p distribution as a function of three radial positions r/R

Numerical and experimental C_p distributions corroborate rather well for the pressure side and show some discrepancies for the suction side. The cases with notable differences are the case with low λ for $r = 0.88R$ (figure 10(a) in purple) and the case with high λ for $r = 0.38R$ (figure 10(b) in dark blue). For low λ (a), the numerical and experimental comparison showed the highest variations for the power and trust coefficients. More specifically at $r = 0.88R$, the numerical C_p distribution shape predicts a high suction peak at the leading edge while the experimental does not. At the other two radial positions, the comparison is more satisfactory. If the numerical simulation predicts higher leading edge suction peaks, it suggests that the induced pressure force could be overestimated, leading to a higher power coefficient and bending moment prediction as observed in figure 8 and in figure 9. However, some differences in the pressure gradient evolution can be observed with a gap that increases towards the trailing edge. For example, the numerical simulation predicts a pressure plateau, signature for full separated flows, whereas the experiment does not. The zoomed area highlights that the AGR mesh tends to improve the pressure gradient prediction along the airfoil compared with the experimental one. Therefore, the prediction of the separation location and detached flow region should be improved with AGR. In addition, for this low λ, the chord-based Reynolds number can be quite low and under 200 000. Reynolds effects that occur may not be so well predicted by the turbulence model chosen for the URANS simulation. For high λ (b), close to the operating point that maximizes the power coefficient, the comparison is more satisfactory as a whole. As expected, flows are less subject to separation and Reynolds effects for the resulting flow velocities experienced by the blade sections.

4. CONCLUSION AND PERSPECTIVES

A comparative study between numerical simulations and experiments to predict the aerodynamic performances of a wind turbine rotor is discussed in this paper. $k-\omega$ SST URANS simulation of a complete rotor, with and without AGR method, is performed. Wind tunnel experiments is conducted on a wind turbine model under turbulent inflow conditions. An encouraging agreement between the experimental and numerical values can be seen for physical variables computed at three scale levels, i.e. airfoil, blade, and rotor scale. Slight discrepancies are particularly noticeable when Reynolds effects and separated flows have to be predicted accurately. Indeed, the right assessment of power and thrust coefficients is highly dependent on this. Furthermore, the AGR meshing tends to improve the prediction of flow conditions at the airfoil scale.

Future work will focus on comparison with DDES simulation data. The comparison will ensure the validity of the code for low turbulent inflow conditions and low chord-based Reynolds number before moving on to increasingly realistic turbulence rates and higher Reynolds number. Another aspect of the research will focus on

the need to model the velocity gradient measured in the wind tunnel. Taking into account the real inlet field in the wind tunnel will help to further explain the observed differences between numerical and experimental results.

5. ACKNOWLEDGMENTS

The authors acknowledge the support of the French Agence Nationale de la Recherche (ANR), under grant ANR-19-CE05-0034 (project MOMENTA). The computations is performed using HPC resources from GENCI (Grand Equipement National de Calcul Intensif) (Grant-A0152A00129) which is gratefully acknowledged. EvoMesure, including Mr. Landolt from Streamwise, is acknowledged for taking measurements in the wind tunnel with the ProCap system.

REFERENCES

[1] P. Veers, C. L. Bottasso, L. Manuel, J. Naughton, L. Pao, J. Paquette, A. Robertson, M. Robinson, S. Ananthan, T. Barlas, A. Bianchini, H. Bredmose, S. G. Horcas, J. Keller, H. A. Madsen, J. Manwell, P. Moriarty, S. Nolet, and J. Rinker. *Wind Energy Sci.*, **8**:1071–1131, 2023.

[2] J. Bartl and L. Sætran. *Wind Energy Sci.*, **2**:55–76, 2017.

[3] G. Chen, X. B. Li, and X. F. Liang. *Energy*, **238**:121772, 2022.

[4] P. Å Krogstad and J. A. Lund. *Wind Energy*, **15**:443–457, 2012.

[5] M. Moshfeghi, Y. J. Song, and Y. H. Xie. *J. Wind Engineer. Indus. Aerodyn.*, **107-108**:94–105, 2012.

[6] M. H. Lee, Y. C. Shiah, and C. J. Bai. *J. Wind Engineer. Indus. Aerodyn.*, **149**:17–29, 2016.

[7] R. Wagner, M. Courtney, J. Gottschall, and P. Lindelöw-Marsden. *Wind Energy*, **14**:993–1004, 2011.

[8] J. Bartl, A. Müller, A. Landolt, F. Mühle, M. Vatn, L. Oggiano, and L. Sætran. *J. Phys.: Conf. Series*, **1104**, 2018.

[9] S. Aubrun, A. Leroy, and P. Devinant. *50th 3AF International Conference On Applied Aerodynamics*, **FP-61**, 2015.

[10] S. Baleriola, A. Leroy, S. Loyer, Ph Devinant, and S. Aubrun. *J. Phys.: Conf. Series*, **1037**:022014, 2018.

[11] C. L. Bottasso, F. Campagnolo, and V. Petrović. *J. Wind Engineer. Indus. Aerodyn.*, **127**:11–28, 2014.

[12] G. B. Deng, P. Queutey, and M. Visonneau. *European Conference on Computational Fluid Dynamics*, **FP-61**, 2006.

[13] J. Wackers, G. Deng, E. Guilmineau, A. Leroyer, P. Queutey, M. Visonneau, A. Palmieri, and A. Liverani. *J. Comp. Phys.*, **344**:364–380, 2017.

[14] G. Comte-Bellott and S. Corrsin. *J. Fluid Mech*, **25**:657–660, 1966.

[15] P. Y. Passaggia, N. Mazellier, and A. Kourta. *Phys. Fluid.*, **33**, 2021.

[16] W. D. Baines and E. G. Peterson. *Trans. Am. Soc. Mech. Engrs.*, **73**:467–477, 1951.

[17] S.A. Hsu, E.A. Meindl, and D.B. Gilhousen. *Journal of Applied Meteorology*, **33(6)**:757–765, 1994.

[18] R. Mishra, E. Guilmineau, I. Neunaber, and C. Braud. [preprint]. *Wind Energy Sci. Discuss.*, doi.org/10.5194/wes-2023-70, 2023.